RESEARCH ARTICLE   OPEN ACCESS

Unraveling Failure Mechanism of Indium Anodes in all-Solid-State Batteries

Haoqi Ren[1,2] | Xiaoting Lin[2] | Jiamin Fu[2] | Yipeng Sun[2] | Xiaozhang Yao[2] | Yingjie Gao[2] | Bolin Fu[2] | Weihan Li[1] | Changhong Wang[1] | Xueliang Sun[1] (ORCID)

[1]Eastern Institute for Advanced Study, Zhejiang Key Laboratory of All-Solid-State Battery, Ningbo Key Laboratory of All-Solid-State Battery, Ningbo Institute of Digital Twin, Eastern Institute of Technology, Ningbo, Zhejiang 315200, China | [2]Department of Mechanical and Materials Engineering, University of Western Ontario, 1151 Richmond Street, London, Ontario, Canada

Correspondence: Weihan Li (whli@eitech.edu.cn) | Changhong Wang (cwang@eitech.edu.cn) | Xueliang Sun (xsun9@uwo.ca)

ABSTRACT

Alloy-based anodes, particularly indium (In) are emerging as promising candidates for achieving long-cycle life in all-solid-state lithium batteries (ASSLBs), due to their dendrite-free characteristics and ability to stabilize the anode interface. However, their practical applications remain hindered by limitations in the failure of In anodes under high current densities and areal capacities, where the incomplete understanding of the underlying failure mechanism limits the optimization strategies. Herein, we employ advanced characterization techniques to systematically investigate the failure mechanisms of In anodes under high current densities and areal capacities. Our findings reveal that alloying and dealloying processes involve an electro-chemo-mechanical coupling failure mechanism and further exacerbate performance degradation. By elucidating these failure mechanisms, our work provides critical insights and rational surface protection strategies by ALD coating with Al_2O_3 layer for enhancing the interfacial stability and performance of alloy anodes in ASSLBs. The maximum cycling capacity of the Li/In asymmetric cell at 0.5 mA/cm^2 was enhanced from 0.2 to 2 mAh/cm^2 (>200 cycles). This work paves the way for the development of durable, high-energy-density batteries.

1 | Introduction

All solid-state lithium batteries (ASSLBs) have emerged as an important technology due to their enhanced safety and higher theoretical energy density compared to conventional lithium-ion batteries using liquid electrolytes [1–3]. In the past ten years, the research community has made giant progress in the field, which is benefited from the development of solid electrolyte with high ionic conductivity [4–9]. Among all the anode candidates, Li metal anode, regarded as "holy grail" anode material, exhibits ultrahigh theoretical capacity (3860 mAh/g) and the lowest redox potential (−3.04 V vs standard hydrogen electrode), which is required to fabricate high-energy-density ASSLBs [10–13].

However, Li metal anodes face significant challenges, including severe interfacial reactions with SSEs and the growth of Li dendrites. These issues contribute to rapid electrochemical performance degradation, internal short circuits, and ultimately, battery failure. To address these challenges, alloy-type anodes have emerged as promising alternatives, offering high theoretical capacities and dendrite-suppressing characteristics [14–17]. Indium (In) alloys stand out among various alloys. Despite the high potential level of In could lead to low energy density of full cells, In anode still becomes the most popular choice in labs due to their excellent mechanical ductility, which ensures tight contact at the anode-electrolyte interface, reducing interfacial resistance. Furthermore, the high charging/discharging
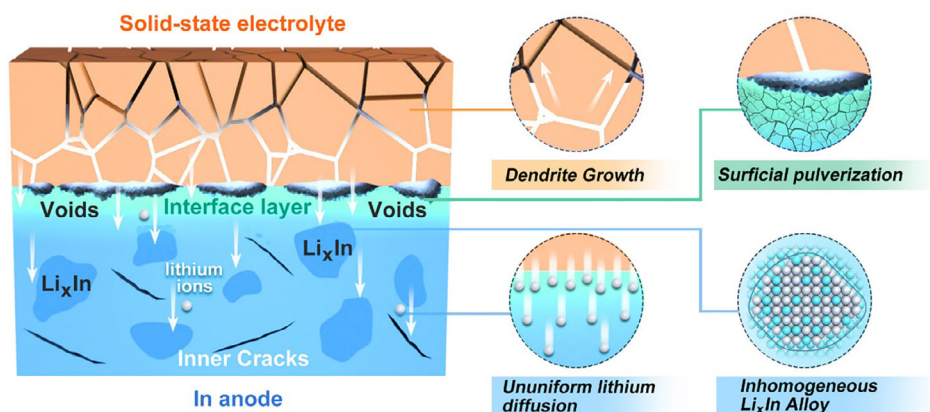
FIGURE 1 | Schematic of the mechanism of In alloy anode failure.

plateau of In alloys mitigates the formation of Li dendrites, enabling a longer cycling life for ASSLBs. These attributes make indium alloy anodes a compelling choice for overcoming the limitations of Li metal anodes and help advance the fundamental understanding of the interaction between anode and SSEs [18, 19].

However, In anode presents fast capacity decay under high current density and high capacity loading due to dendrite growth and surficial degradation. Despite some findings of the optimization of Li-In alloy anodes have been made, the mechanisms underlying dendrite formation in In anodes remain inadequately understood. For instance, Luo et al. manifested that Li-In dendrite could grow along with boundaries due to interfacial reactions at high current density and high loading, and finally cause the short circuit [20]. Moreover, it was also emphasized that the carrier transition from Li ions to Li atoms on the interface would lead to the formation of a Li-rich phase at the surface and slow down the diffusion [21, 22]. In short, the previous work predominantly focused on the stability of the anode-SSE interface, while the effects of alloying and dealloying processes on anode stability have received limited attention. Besides, studies investigating dendrite growth often apply current densities exceeding the critical limits of SSEs to observe dendritic behaviors, overlooking the dendrite growth mechanisms relevant under long-term cycling conditions in practical applications. Moreover, soft breakdown behaviors, which are another critical factor influencing the operational life of ASSLBs, have not been thoroughly examined [23–25]. A comprehensive understanding of the origins of anode failure is therefore essential to advancing the fundamental knowledge of alloy anodes and enabling their interfacial design in ASSLBs.

In this work, we systematically investigated the failure mechanism of In anode under different current density and areal capacity via a Li/Li$_6$PS$_5$Cl (LPSC)/In asymmetric cell. We unraveled high current density- and high areal capacity-driven failure mechanisms by scanning electron microscopy (SEM). Under high areal capacity conditions, In anodes undergo serious interfacial reactions with SSEs and are pulverized due to the stress from inhomogeneous Li deposition. Under high current densities, soft shorts typically occur first, and their gradual accumulation ultimately leads to hard shorts in ASSLBs. This

behavior can be attributed to the interfacial diffusion barrier and the limited mobility of Li atoms in the anode, as shown in Figure 1. According to the intrinsic failure mechanisms, an interface modification strategy of In anode via ALD coating significantly improved the electrochemical performance of the asymmetric cells. The introduction of a protection layer significantly improved the performance of the Li/In asymmetric cell at 0.5 mA/cm^2, increasing the capacity from 0.2 to 2 mAh/cm^2 and enabling stable cycling for at least 200 cycles. Additionally, the lifetime of the LCO/LIC/LPSC/Li-In full cell was extended to twice that of the uncoated counterpart. This work offers new insights into the failure mechanisms of alloy anodes and contributes to the development of more effective anode–SSE interfacial designs.

2 | Results

Li-In or pristine In anodes are commonly used in ASSLBs in current research, and they would exhibit a similar electrochemical alloy mechanism. As shown in Figure S1a, Li-In alloy could form at the interface between In and LPSC, and Li would diffuse into the further end of In anode over time. A typical preparation of Li-In alloy anode is to compress the In foil together with thin Li foil, and the alloy mechanism is shown in Figure S1b [26, 27]. When a Li foil is applied in the battery, the diffusion of Li could come from both ends and thus provide additional Li during stripping. The electrochemical behavior of the asymmetric batteries without Li foil at 0.1 mA/cm^2–0.2mAh/cm^2 is shown in Figure S1c. The batteries using In anode could run stably in the initial 50 cycles. On the contrast, the electrochemical behavior of batteries with Li foil is shown in Figure S1d. The cycling performance was similar to that without Li foil, indicating the plating and striping behavior are almost the same in the pristine In and Li-In alloy anode. The major difference between the two anodes came from CE (Figure S1e,f). The CE was never lower than 100% since the excess Li provided by Li foil could compensate for the Li loss in the irreversible reaction. Therefore, Li-In alloy anode is supposed to go through the same mechanism as In anode, while it could have a better performance in full cells. In order to directly observe the failure reason of the In alloy anode, we focus on the performance of the pristine In anode without the interference of additional Li.

2.1 | Influence of Areal Capacity

The alloying mechanism of the Li-In anode can be described by a reconstitution reaction of Li_xIn phases between Li and In. The lithiation process is shown by a Li/LPSC/In asymmetric cell in Figure S2a. It went through a phase transition depending on the deposited Li amount. The three distinct voltage plateaus at 0.62, 0.29, and 0.01 V during the Li–In alloying process correspond to a series of Li–In phases. When the plating areal capacity was smaller than 6.5 mAh/cm^2, a flat plateau appeared as a result of the formation of a stable mixed phase of In/LiIn. Then the second and third plateaus occurred at the areal capacity of 7.1 to 8.9 and > 9.1 mAh/cm^2 represented the phase of $LiIn/Li_5In_4$ and Li_5In_4/Li_3In_2, respectively. The cycling performance of the asymmetric cell with the capacity of 10 mAh/cm^2 was also tested, as shown in Figure S2b. The battery failed in the second cycle as it cannot release the lithium in the alloy phase, confirming that the areal capacity has a significant influence on the lifespan of the battery.

The cycling performance with different areal capacities was tested at the current density of 0.1 mA/cm^2 in Figure 2. When cycled at a low areal capacity of 0.2 mA/cm^2 (Figure 2a), the cell maintained stable operation without any failure for over 1500 h. In this configuration, the low Li deposition resulted in the formation of an In/LiIn phase on the In anode surface, exerting a negligible impact on its structure. The charge–discharge profile confirms the cycling stability. The charging-discharging curve of the 50th and 250th cycles, corresponding to the accumulated areal capacity of 10 and 50 mAh/cm^2 are shown in Figure S3a. It can be found that there was almost no change of curves between the 49th and 50th, or 249th and 250th cycle, implying the overpotential was almost the same during cycling. The stable overpotential indicated that there were no apparent cracks or contact loss, which increased the interfacial resistance. Moreover, the CE could be kept over 97.5% during stable cycling, as shown in Figure S3d. The efficiency of the asymmetric cell lower than 100% can be attributed to it that part of the lithium will be irreversibly "locked" in the In anode [26]. It would be fatal in a full battery since Li loss would lead to the irreversible degradation of the cathode.

The influence of areal capacity was further explored by enhancing the areal capacity per cycle. The cycle performance of Li/LPSC/In with 1 mAh/cm^2 is shown in Figure 2b. It was found that stable performance could be maintained for over 1200 h at the higher areal capacity. Notably, the polarization voltage increased with each cycle, indicating a continuous rise in interfacial resistance (Figure S3b). This trend can be partially attributed to low-conductivity phases formed by interfacial reactions or to cracks induced by dendritic growth [28–30]. The CE was 97.9% in the first cycle and then gradually increased to 99.3% in the first 10 cycles (Figure S3e). It was attributed to an activation process that In anode would form Li_xIn phase. Then, it appeared a descending tendency after about 30 cycles, indicating the irreversible phase transformation. When the areal capacity was increased to 5 mAh/cm^2, the cycling would be much more unstable as shown in Figure 2c. An apparent increase in polarization voltage occurred. It could be found that the voltage gap between charging and discharging plateau was 33.4 and 250.1 mV when the accumulated

areal capacity reached 10 and 50 mAh/cm^2 as shown in Figure S3c (second and 10th cycle). This large overpotential would slowly lead to battery failure. The change in CE also manifested the tendency in Figure S3f. The CE could be relatively stable at around 97.5% in the first 4 cycles, and it had a small decrease in the fifth cycle. Finally, it fast dropped to 92.4% in the 10th cycle, implying a severe irreversible reaction.

2.2 | Influence of Current Density

The critical current density (CCD) of the asymmetric cell is 0.8 mA/cm^2, as shown in Figure S4. Thus, the influence of current density is also investigated at 0.2 mA/cm^2 (low), 0.5 mA/cm^2 (high), and 1 mA/cm^2 (above the CCD) at a constant areal capacity of 0.2 mAh/cm^2. In Figure 2d, the cell cycled at 0.2 mA/cm^2 exhibited stable performance, whereas the cell cycled at 0.5 mA/cm^2 experienced severe voltage fluctuations—indicative of a soft breakdown—after approximately 20 h. When the soft breakdown occurred, carrier transfer would be achieved by both electronic and ionic current flow [24]. Though this soft short would be partially recovered during cycling, it would still lead to battery failure due to overcharge [23, 25]. When the current density increased to 1 mA/cm^2, the occurrence of soft breakdown would be much earlier, suggesting that high current density had significantly influence on the dendrite growth in In anode. Moreover, the soft short will easily transform into a hard short, resulting in a persistent internal short circuit failure due to the dendrites penetration. The charging-discharging voltage profile of the batteries at different current density is shown in Figure S5a. After cycling to an accumulated areal capacity of 2.4 mAh/cm^2 (12th cycle), the electrochemical behavior diverged markedly. At 0.2 mA/cm^2, the voltage profile remained stable, whereas the cell cycled at 0.5 mA/cm^2 exhibited a more rapid decay in charging

When the areal capacity per cycle increased to 0.5 and 1 mA/cm^2 rapid shorting occurred—especially at high current densities (Figure S6)—indicating that elevated current density combined with large areal capacity accelerates failure. Notably, a Li/LPSC/Li–In cell cycled at 0.5 mA/cm^2 with an areal capacity of 0.2 mAh/cm^2 (Figure S7a) underwent an activation process during the first ten cycles, after which its cycling stability was significantly enhanced compared to the pure In anode. The Coulombic efficiency (Figure S7b) indicates that this activation corresponds to an alloying reaction, maintaining ~97.5% efficiency over subsequent cycles. Therefore, pre-lithiation of the In anode appears to be an effective strategy for improving its cycling performance.

Based on the voltage profiles of different areal capacity and current density, an electro-chemical diagram of the failure mechanism could be depicted in Figure 2e. The failure mechanism map is divided into four parts based on a great deal of reproducible experimental data: fast hard short-circuit (red region), fast impedance increase (yellow region), slow impedance increase (green region) and stable region (blue region). When the current density and areal capacity are high (> 0.5 mA/cm^2 and > 1mA/cm^2), the battery failure could be attributed to the fast short-circuit aroused from a synergistic effect of dendritic growth and interfacial reactions. The lifespan of batteries cycled
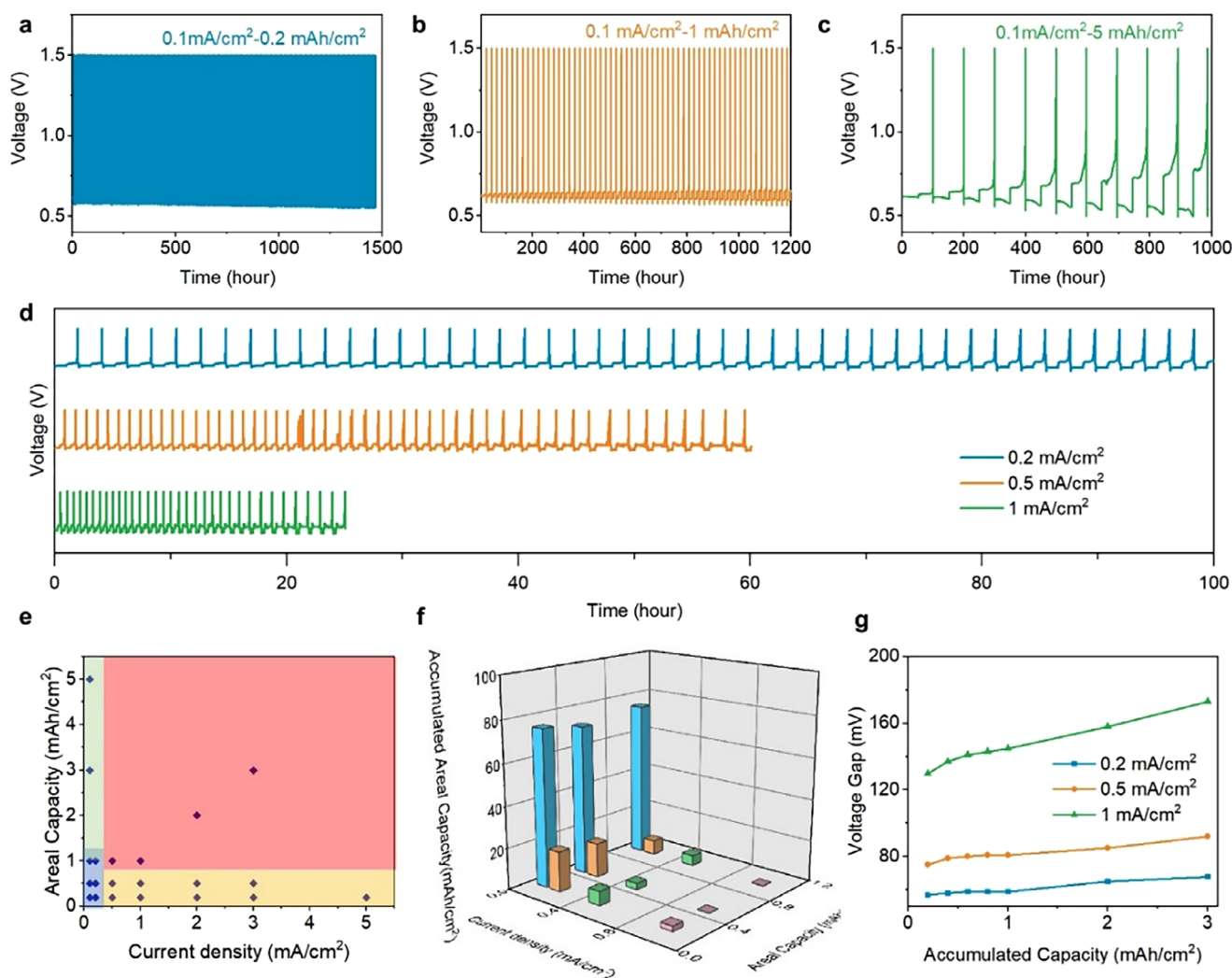
FIGURE 2 | Electrochemical performance of Li/LPSC/In asymmetric cell with different areal capacity cycled and different current density (a) Cycling performance of asymmetric cell at the capacity of 0.2 mAh/cm^2 at 0.1 mA/cm^2. (b) Cycling performance of an asymmetric cell at a capacity of 1 mAh/cm^2 at 0.1 mA/cm^2. (c) Cycling performance of an asymmetric cell at a capacity of 1 mAh/cm^2 at 0.1 mA/cm^2. (d) Cycling performance of Li-In asymmetric cell at 0.2, 0.5, and 1 mA/cm^2 at the capacity of 0.2 mAh/cm^2. (e) Failure mechanism map showing the stability of Li-In asymmetric cell (blue area: stable cycling; yellow area: slow failure with high polarization; green area: fast failure with soft short; red area: ultrafast failure with hard short). (f) Electrochemical diagram of the accumulated capacity (lifespan) at different electrochemical behaviors. (g) voltage gap change at different accumulated areal capacity of the Li-In asymmetric cell at 0.2, 0.5, and 1 mA/cm^2 at the capacity of 0.2 mAh/cm^2.

at different current density and areal capacities is also given in Figure 2f. When the current density is low (0.1 mA/cm^2), the accumulated areal capacity before failure is higher than 60 mAh/cm^2 and the areal capacity in single cycle has almost no impact on the lifespan. When the current density increases, failure easily occurs especially at high areal capacity. Therefore, the lifespan of batteries majorly depends on the current density than the areal capacity. The CE in Figure 3c,d reflects the tendency as well. When the current density was set at 1 mA/cm^2, an apparent soft breakdown can be found as voltage fluctuation during charging process. Further analysis was made on the voltage gap as shown in Figure 2g. The voltage gap in the initial cycle reflects the resistance of cell configuration. The voltage gap of batteries cycled at 0.2 and 0.5 mAh/cm^2 were stable in the first 5 cycles and had a slight increase in the following 10 cycles, while that of battery cycled at 1 mA/cm^2 will have a continuous increase since the first cycle. The tendency in nucleation overpotential

change verifies that the increased resistance would be ascribed to the inhomogeneous deposition of Li as shown in Figure S5b. For the battery cycled at 0.2 mA/cm^2, the nucleation overpotential had no significant change; The nucleation overpotential of the battery cycled at 0.5 mA/cm^2 would gradually increase after the occurrence of soft breakdown. A significant increase occurred in the first cycle in the battery cycled at 1 mA/cm^2, indicating the plating behavior is much more different from that in batteries cycled at low current density and excess Li deposition would lead to the high overpotential [31].

In Figure S5c, the CE at different areal capacity was tested at the current density of 0.1 mA/cm^2. It could be found the initial CE is lower at higher areal capacity because of a higher degree of alloy reaction between Li-In, and it would gradually increase to a steady level. Then the CE of batteries cycled at 5 mAh/cm^2 will significantly decrease, suggesting a fast failure
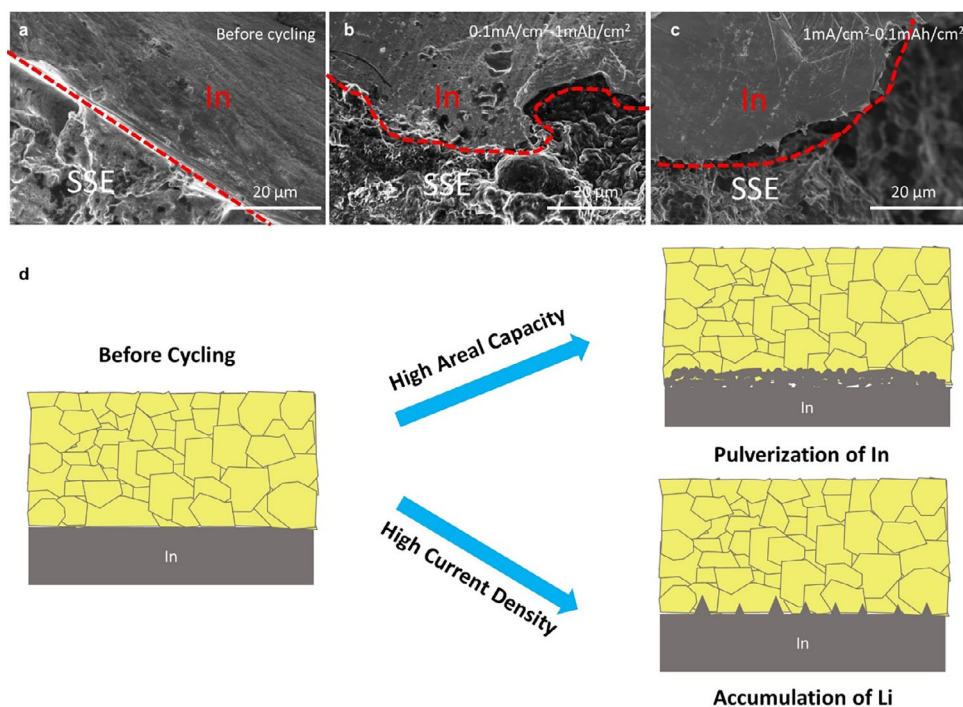
FIGURE 3 | Morphological evolution of In anode (a) Cross-section SEM image of LPSC-In before cycling. (b) Cross-section SEM image of LPSC-In cycled at 0.1 mA/cm^2–1 mAh/cm^2 (accumulated areal capacity is 10 mAh/cm^2). (c) Cross-section SEM image of LPSC-In cycled at 1 mA/cm^2–0.1 mAh/cm^2 (accumulated areal capacity is 10 mAh/cm^2). (d) Schematic of the morphological evolution under high areal capacity and high current density.

would occur in such high areal capacity. In Figure S5d, the CE at different current density was tested at 0.2 mAh/cm^2. An abnormal CE could be observed when the current density is 0.5 and 1 mAh/cm^2, indicating the occurrence of a short-circuit [32, 33]. Thus, dendrite growth could be the major reason of the rapid failure in high current density.

Additionally, Li-In alloy/LPSC/In asymmetric cell configuration was also used to evaluate the cycling performance. As shown in Figure S8a, the cell was tested under different areal capacity as well as current density. The cell could run relatively stable at 0.2 mA/cm^2–0.2 mAh/cm^2, however, the CE continuously decreased as shown in Figure S8b. After 50 cycles, the CE decreased to 88% much lower than that in the cell using a Li metal anode. It indicates the Li reversibility is poorer than, which would induce an electrode structure degradation. It becomes more apparent especially at high areal capacity, and a fast failure occurred when the battery cycled at 0.5 mA/cm^2–0.5 mAh/cm^2 and 1 mA/cm^2–1 mAh/cm^2. Despite Li-In anode easily failed at high areal capacity, no obvious soft breakdown was found in the cell cycled at 1 mA/cm^2–0.1mAh/cm^2 for 100 cycles in Figure S8c, suggesting that Li-In can relieve dendrite penetration compared with Li metal.

3 | Discussion

3.1 | Different Electrochemical Failure Mechanism

In order to explore the failure mechanism of In anode, SEM is applied to confirm the morphological evolution under different

conditions. The interface between LPSC and indium would exhibit obvious differences after cycling, as shown in Figure 4a–c. In Figure 4a, the interface between the LPSC and In anode was distinct and flat. When the cell was cycled at 0.1 mA/cm^2 with the capacity of 1 mAh/cm^2, the interface became quite rough after the accumulated areal capacity of 10 mAh/cm^2, and the indium anode was severely "etched" in an ununiform shape (Figure 4b). This etching process arose from the interfacial reaction occurring at the In alloy anode. The composition of the SEI was identified by XPS. As shown in Figure S9a, two 3d$_{5/2}$ peaks appear in the In 3d spectrum. The peak at 444.6 eV corresponds to the formation of InP, while the peak at 451.2 eV indicates the presence of In$_2$S$_3$. The S 2p spectrum in Figure S9b also shows peaks at 160.2 and 161.5 eV, which are attributed to Li$_2$S and In$_2$S$_3$, respectively. Furthermore, P (130.3 eV) and InP (128.6 eV) were further observed in FigureS9c, which is in accordance with In 3d spectrum. Hence, the side reaction between In anode LPSC during cycling will significantly alter the morphology of the interface and result in the surficial pulverization at high areal capacity. EDAX mapping showed the distribution of In in Figure S10a–c. It could be found the In would be porous and unevenly distributed, indicating the degradation of the structure of the anode. On the contrast, the In anode under 1 mA/cm^2–0.1 mAh/cm^2 had small micro- Li$_x$In dendrites but still kept a smooth surface (Figure 4c). In Figure S10d,e, the mapping showed that the dendrites contain the indium, indicating the formation of Li$_x$In dendrites can be attributed to the mobility of In atoms during cycling.

The morphological evolution under two representative cycling conditions was examined at varying accumulated areal capacities. SEM images of the cell cycled at 0.1 mA/cm^2 with 1 mAh/cm^2 per
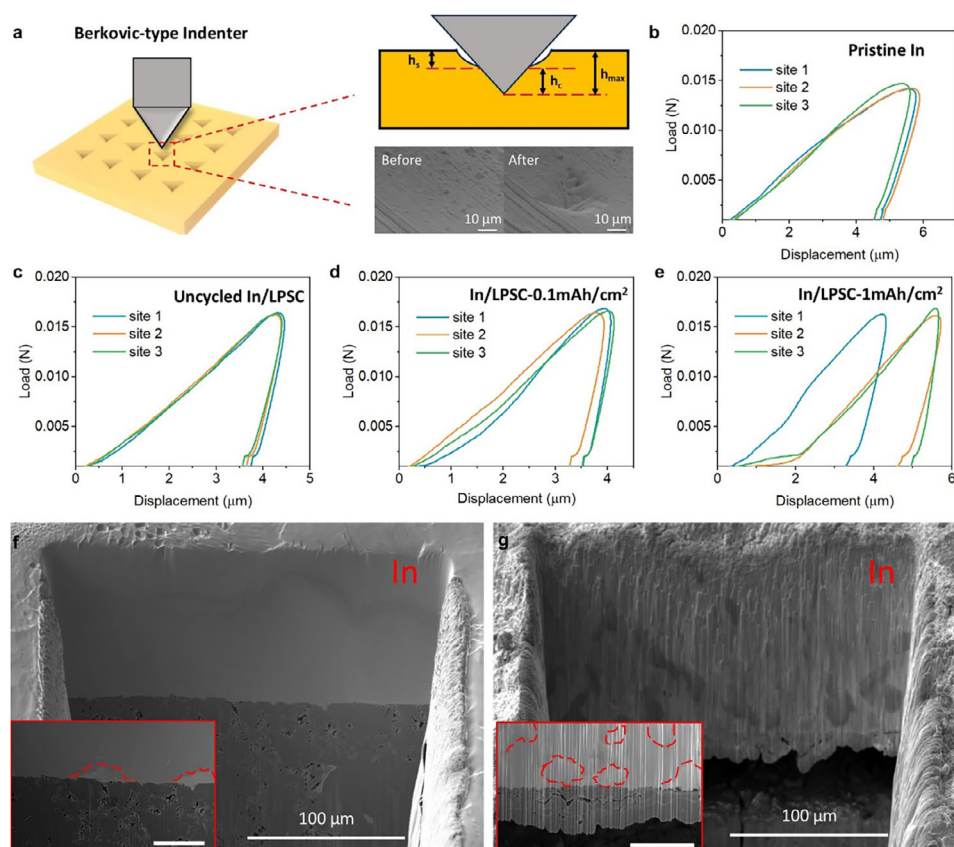
FIGURE 4 | Inhomogeneous deposition in In anode (a) Schematic of the nanoindentation SEM setup. (b) Nanoindentation test on different sites on pristine In. (c) Nanoindentation test on different sites on In anode before plating. (d) Nanoindentation test on different sites on In anode with plating 0.1 mAh/cm^2 of Li. (e) Nanoindentation test on different sites on In anode with plating 1 mAh/cm^2 of Li. (f) Cross-section image of In anode after plating 1 mAh/cm^2 of Li. (g) Cross-section image of In anode after plating 5 mAh/cm^2 of Li.

cycle are shown in Figure S10a–c, corresponding to accumulated capacities of 1, 2, and 5 mAh/cm^2, respectively. As cycling progressed, the In foil edge became increasingly jagged, and an interfacial alloy layer formed, whose thickness grew with further cycling. In contrast, for cells cycled at 1 mA/cm^2 with 0.1 mAh/cm^2 per cycle, the interfacial structure remained relatively smooth at accumulated capacities of 1 and 2 mAh/cm^2 (Figure S11a,b). Small dendrites would occur on the top surface when the accumulated areal capacity increased to 5 mAh/cm^2 (Figure S11c). The influence of applied external pressure (125, 250, and 500 MPa) was also investigated in the cells cycled at 1 mA/cm^2–0.1 mAh/cm^2 as shown in Figure S13a–c, respectively. Both the amount and size of lithium-indium dendrites decreased at 125 MPa (Figure S13a). Further, the contact between LPSC and In anode became much closer, and no apparent filament was observed. However, the cell quickly failed when the pressure rose to 500 MPa, and sphere-like dendrites occurred on the pulverized surface. The fast failure could be attributed to the cracks at the inner part of solid electrolytes, which was induced by the high pressure. The voids would lead to an uneven local current density and lead to dendrite penetration [34]. Therefore, the degradation modes of the In anode are summarized in Figure 3d. When cycled at low current density but high areal capacity, anode failure originates from In foil fracture. In contrast, at high current density with low areal capacity, lithium accumulates at the interface, and failure is dominated by dendrite growth. Fractures may even appear far from the anode–SSE interface. For example, after

cycling to an accumulated capacity of 10 mAh/cm^2 at 0.1 mA/cm^2 (1 mAh/cm^2 per cycle), a large crack appears deep within the anode, distant from the interface (Figure S14a). Conversely, many fine cracks are observed in the anode cycled at 1 mA/cm^2 with 0.1 mAh/cm^2 per cycle (Figure S14b). These fractures result from internal stress induced by phase transitions during cycling [35]. Thus, it suggests that high areal capacity in each cycle would have an apparent influence on the mechanical properties of the anode and finally lead to cracks and failure.

3.2 | Origin of Mechanical Failure

To further explore the origin of anode fracture at high areal capacity, a nano-indentation test was applied as shown in Figure 4a. A Berkovic-type indenter was pressed on the anode to test the indentation hardness by recording the indentation depth, height of elastic deformation, and height of inelastic deformation [36]. The test was conducted on three random sites of pristine In in Figure 4b, and it shows that the pristine In is flat and the hardness of different sites are almost the same. The interface of LPSC/In before cycling was also tested by peeling In off from the SSE pellet. In this case, the displacement-load curves at random sites are still in the same shape (shown in Figure 4c), indicating that the interfacial chemical reaction was homogeneous and had little influence on changing the surface structure. The surface of In anode with plating 0.1 and 1 mAh/cm^2 at 0.1 mA/cm^2 are tested

in Figure 4d,e, respectively. The displacement at the same load in Figure 4d begins to show a slight difference, indicating the fracture begins. The slope of recovery curves (in the red box) reflects that the mechanical strength, e.g., Young's modulus, has no obvious change. When the amount of deposited Li increased to 1 mAh/cm^2, the differential in displacement became larger as shown in Figure 4e, and it evidenced an inhomogeneous Li deposition because of structural degradation occurred along with the plating process. Moreover, the slope at site 3 is apparently increased, suggesting the formation of a stiffer phase. The stiffer phase could be attributed to the new Li$_x$In alloy phase. As shown in Figure S15, the DFT calculation presents that the excess introduction of Li in the alloy phase will enhance the stiffness of the lattice. Consequently, the Young's modulus of pure In is 38.7 GPa, while the In$_4$Li$_5$ and In$_2$Li$_3$ is 44.5 and 60.7 GPa, respectively. Therefore, the anode will become brittle and thus lead to the crack of anode when it forms In$_2$Li$_3$ phase. Ideally, the In$_2$Li$_3$ phase should only form when all the In transforms into In$_4$Li$_5$ (orange area in Figure S2a). However, the In$_2$Li$_3$ phase would form in advance when the plating is inhomogeneous. FIB-SEM was used to observe the partial fracture in the anode after cycling in Figure S15. For the uncycled LPSC-In pellet, the In anode is homogeneous in Figure S16. When plating 0.785 mAh Li (1mAh/cm^2) into the anode, the In near the LPSC will form Li$_x$In alloy, while the far end of In remains the same (Figure 4f). In order to identify the formed phase, ex situ XRD was conducted by peeling off In foil after cycling. As shown in Figure S17, the major peak at 30.1° was attributed to the LPSC residue, while the peak at 37.3° represented the formation of In$_2$Li$_3$ phase. As a result, two phases with different contrasts could be observed. Furthermore, small bright flakes could be observed, which would be the anode fracture due to the inhomogeneous deposition and alloy reaction. When the plating amount of Li reached 3.85 mAh (5 mAh/cm^2), the interface will crack due to the large differential in mechanical stress and more inhomogeneous Li$_x$In alloy will occur at the surface of In anode (Figure 4g).

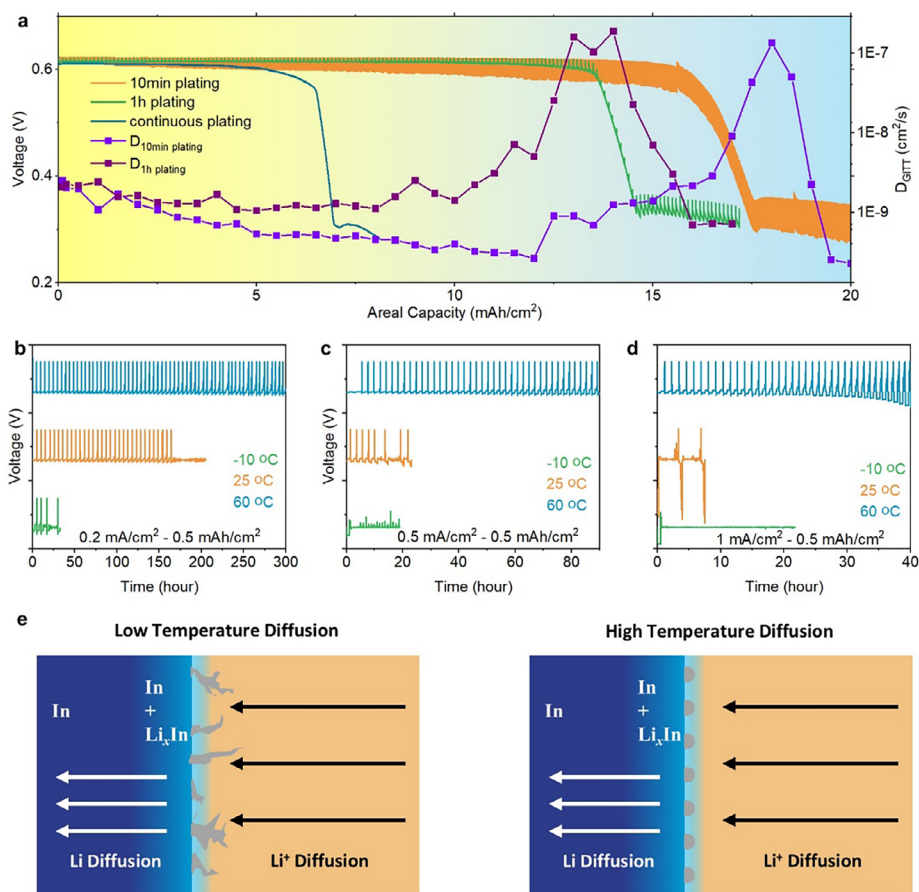## 3.3 | Diffusion Limitations

A galvanostatic intermittent titration technique (GITT) was performed with different amounts of Li plated per pulse to investigate the kinetic and thermodynamic influences. As shown in Figure 5a, when 0.017 mAh/cm^2 of Li was plated each pulse (10 min plating), the first LiIn-phase plateau appears at an accumulated areal capacity of 15.57 mAh/cm^2, and the second plateau begins at 17.44 mAh/cm^2 (orange curve). However, the one with 0.1 mAh/cm^2 Li plated (plating 1 h) each pulse and continuous plating has the first plateau of 6.45 (cyan line) and 13.50 mAh/cm^2 (green line) and second plateau beginning at 6.99 and 14.49 mAh/cm^2, respectively. Therefore, the interfacial phase transitions markedly affect the anode's maximum capacity. Furthermore, the observed increase in overpotential during each 10 min plating pulse indicates that the interfacial phase composition changes with varying plating amounts per cycle. The diffusion constant of Li in the anode (D$_{GITT}$) is also calculated. It could be found the two initial D$_{GITT}$ are almost at the same level since the diffusion constant is an intrinsic property when the temperature is constant. Along with the accumulated amount of Li increases, D$_{10 min}$ slowly descended, but D$_{1h}$ remained stable

until the plating amount reached 8 mAh/cm^2. Then both two D increased at the end of the first plateau and decreased at the beginning of the second plateau. It is calculated that the stable region corresponds to a stable Li atom diffusion coefficient D of 10^{-10} cm^2/s and can reach the highest D more than 10^{-7} cm^2/s when the voltage decreased (phase transition area). Therefore, the phase transition kinetics will significantly influence the diffusion process. Moreover, D$_{10min}$ and D$_{1h}$ reached the maximum value at different stages, which would indicate an inhomogeneous phase transition when applying different plating conditions. Then the diffusion coefficient reduced again in the second plateau, which should be attributed to low diffusion ability in highly lithiated In phase [37].

Temperature will significantly influence the diffusion kinetics in In anode. Herein, the cycling performance of high temperature (60°C) and low temperature (−10°C) are investigated at different current density. Figure 5b–d shows the cycling performance of batteries cycled at 0.2, 0.5, and 1 mA/cm^2 with the areal capacity of 0.5 mAh/cm^2, respectively. As shown in Figure 5b, the accumulated areal capacity of the battery cycled at 60 °C was about 22.5 mAh/cm^2, which was the highest among the three temperatures. Soft breakdown occurred at room temperature and result in the short lifespan of batteries. When the temperature went lower, the soft breakdown occurred much earlier. When the current density increased to 0.5 mA/cm^2, the battery cycled at −10°C failed directly in the first cycle, and the cycling performances of batteries cycled at 25°C and 60°C significantly decreased (Figure 5c). When the current density was further increased to 1 mA/cm^2, only the cell cycled at 60°C could work as shown in Figure 5d.

Temperature strongly affects diffusion kinetics in the In anode. Here, the cycling performance at elevated (60°C) and reduced (−10°C) temperatures was evaluated under various current densities. Figure 5b–d present the cycling behavior of cells operated at 0.2, 0.5, and 1 mA/cm^2, each with an areal capacity of 0.5 mAh/cm^2. As shown in Figure 5b, the cell cycled at 60°C achieved an accumulated areal capacity of approximately 22.5 mAh/cm^2— the highest among the three temperatures. In contrast, a soft breakdown occurred at room temperature, leading to a shortened lifespan. At −10°C, soft breakdown manifested even earlier. When the current density was increased to 0.5 mA cm^{-2} (Figure 5c), the cell at −10°C failed within the first cycle, and the performance at 25°C and 60°C also deteriorated significantly. Upon further increasing the current density to 1 mA/cm^2 (Figure 5d), only the cell cycled at 60°C maintained stable operation. Notably, the impedance gradually increased after 30 h, suggesting a stronger interfacial reaction and phase transition at high temperature. In order to investigate the diffusion limitations in the cell, SEM images of the cross-section view of batteries cycled at −10°C and 60°C are shown in Figure S18. Small Li dendrites rather than Li$_x$In directly grew on the surface of the In anode when the battery was cycled at 1 mA/cm^2–0.1 mAh/cm^2 (Figure S18a), while a thick porous interphase would form at the surface the battery was cycled at 0.1 mA/cm^2–1 mAh/cm^2 (Figure S18b). It can be attributed to the low diffusion kinetics of Li in In, and thus Li atoms will accumulate at the surface of the anode and form either a dendrite or react with LPSC to form an interphase based on the current density. On the contrast, the surface of anode cycled at 11 mA/cm^2–0.1 mAh/cm^{2}was flatter only with tiny Li$_x$In

FIGURE 5 | Diffusion Limitations of Li in In (a) GITT profile of Li-In cells with different plating capacity of Li. (b) Temperature-dependent cycling performance of Li-In cycled at 0.2 mA/cm²–0.5 mAh/cm². (c) Temperature-dependent cycling performance of Li-In cycled at 0.5 mA/cm²–0.5 mAh/cm². (d) Temperature-dependent cycling performance of Li-In cycled at 1 mA/cm²–0.5 mAh/cm². (e) Schematic of the temperature-dependent diffusion process of Li from the surface of In anode to the inner part of In anode.

dendrites (Figure S18c) compared with the anode cycled at low temperature. Additionally, the anode surface cycled at 1 mA/cm² with 0.1 mAh/cm² per cycle exhibits smaller cracks and less pulverization (Figure S18d). Therefore, rapid diffusion at elevated temperature promotes a more homogeneous phase transition. The overall influence of diffusion is summarized in Figure 5e. At low temperatures, Li⁺ diffusion through LPSC greatly exceeds Li diffusion within the In anode. Consequently, only a small fraction of plated Li diffuses into the anode to form the alloy, while most Li deposits and accumulates on the anode surface, where its growth is governed primarily by current density. At elevated temperatures, Li diffusion in the anode enables uniform deposition and yields more homogeneous phase transitions. Therefore, enhancing Li diffusion coefficients within the alloy anode is critical in battery design to accommodate high current densities and areal capacities.

3.4 | Interfacial Reaction

Since LiIn anode is not intrinsic stable to LPSC, SEI would form at the interface between anode and LPSC and therefore alter the physiochemical properties of the interface [20, 38]. It may potentially form voids and enhance the local current density, consequently leading to the failure of batteries. In order to figure

out the influence of interface reaction, we introduce an ultrathin stable Al_2O_3 interlayer via the atomic layer deposition (ALD) method. The introduction of the Al_2O_3 layer will insulate the electrode and electrolyte and thus avoid the formation of SEI. The cycling performance of Li-In asymmetric cell at 0.2 mA/cm²–1 mAh/cm² is shown in Figure S19a. A stable cycling for more than 2000 h cycling can be achieved by using the Al_2O_3 coated In anode, while the pristine anode could only work for about 100 h. The CE of the asymmetric cell is also given in Figure S19b. In the first cycle there is an activation process which is similar to the uncoated In anode. Then the CE was stable at 99.5% without an apparent decrease. It evidences that the CE decrease would majorly be caused by the electrochemical interfacial reaction between the Li_xIn alloy and LPSC. The asymmetric cell was also tested under a relatively critical condition 0.5 mA/cm²–2 mAh/cm² as shown in Figure S19c. The cell could run stable for more than 50 cycles, and the CE could be kept at 99.7% as shown in Figure S19d. A cross-section image of the anodes after cycling at 0.2 mA/cm²–1 mAh/cm² is shown in Figure S20. For the unprotected anode, the anode had a strong interfacial reaction with LPSC and thus was electrochemically etched (Figure S20a). On the contrast, the edge of the Al_2O_3-coated In anode is relatively smooth after cycling, though there are still tiny cracks due to the mechanical deformation during phase transition (Figure S20b). The presence of a protective layer before and after

cycling was further identified by Time-of-Flight Secondary Ion Mass Spectrometry (Tof-SIMS). As shown in Figure S21a,b, the Al_2O_3 was uniformly coated on the In anode with an ultrahigh coverage. Figure S21c shows the 3D reconstruction of elemental distribution, revealing the top layer was fully composed of Al_2O_3. Figure S21d,e suggests most parts of the Al_2O_3 layer remained on the surface, though a small part of In were exposed. The crack of the Al_2O_3 layer may result from the destructive peeling-off procedure. The 3D reconstruction of samples after cycling also indicates the ALD coating effectively protected the top surface of In anode and survived during cycling.

Full batteries paired with $LiCoO_2$ (LCO) are used to examine the effectiveness of insulate layer as well. As shown in Figure S18a, three different anodes (pristine In, pristine In/thin Li foil, and Al_2O_3-coated In/thin Li foil) were tested at 0.2 C. The pristine In anode had poor cycling performance, and the discharge capacity decayed from 119.9 to 24.7 mAh/g. It had the lowest initial CE (82.9%) due to the irreversible phase transition in the anode, which led to deterioration of the cathode structure and consequently failed. When introducing excessive Li in the anode, both the initial CE and cycling performance of ASSLB had a significant improvement. The initial discharge capacity was almost the same as the pristine In anode, while it could remain 45.9 mAh/g after 40 cycles. The introduction of the Al_2O_3 layer could furthermore enhance the cycling stability and lifespan. A highest initial CE was achieved and kept at around 98.1% for more than 60 cycles. The charging-discharging curve furthermore demonstrates the effectiveness of the Al_2O_3 layer, as shown in Figure S18b–d. The initial charging-discharging of three batteries are almost similar, while the plateau voltage of the cell using pristine In anode significantly changed, reflecting the polarization is gradually severe every cycle (Figure S18b). The introduction of excessive Li will help reduce the polarization while still having large capacity decay in the first 3 cycles (Figure S18c). The capacity decay was minimized in the cell using an Al_2O_3-coated In anode (Figure S18d). Therefore, the protective layer could effectively inhibit the undesired interfacial reaction and enhance the cycling lifetime of full batteries.

4 | Conclusion

In this study, we systematically evaluated the cycling performance and morphological evolution of In anodes under various electrochemical conditions. High current densities promote dendritic growth, leading to rapid cell failure, whereas high areal capacities induce crack formation and pulverization. These distinct failure modes arise because the electrochemical conditions dictate the underlying chemical reactions, resulting in pulverization, dendrite penetration, or uncontrolled interfacial reactions. Nanoindentation, SEM, and GITT analyses further reveal that the fundamental causes of failure can be classified as poor physical contact, diffusion limitations, mechanical degradation, and interfacial instability. Consequently, enhancing Li diffusivity—by operating at elevated temperatures or introducing an insulating interfacial layer—can significantly improve cell performance. Our findings not only elucidate the intrinsic failure mechanisms of In anodes but also provide practical strategies for optimizing high-energy-density alloy-anode-based ASSLBs. We anticipate that this work will advance the fundamental understanding of

failure in In and other commercial alloy anodes and guide the design of more robust ASSLB configurations.

5 | Methods

5.1 | Materials

Li_6PS_5Cl and In foil were supplied from GLABAT Solid-State Battery Inc. Li_3InCl_6 was synthesized as in our previous paper [8]. Stoichiometric amounts of lithium chloride (LiCl, Alfa Aesar, 99.9% purity) and indium chloride ($InCl_3$, Alfa Aesar, 99.99% purity) were dissolved in deionized water and subsequently dried under vacuum to yield the precursor hydrate. This precursor was then subjected to thermal treatment at 200°C for 4 h under vacuum conditions to synthesize Li_3InCl_6.

5.2 | ALD Coating Procedure

In foils were cut into ~10 mm disks and thoroughly polished to remove any surface oxidation layers. The surface coating of ALD Al_2O_3 was carried out in an Arradiance Gemstar-8 ALD system, which is coupled with an Argon-filled glovebox to avoid air and moisture. The deposition temperature for Al_2O_3 is 120°C, and the precursors are stored in separate stainless-steel bottles to avoid exposure to the air atmosphere. Trimethylaluminium (TMA) and water (H_2O) were used as precursors for Al_2O_3 deposition. Both TMA and H_2O were held at room temperature, which is appropriate to guarantee adequate vapor pressure. A single ALD cycle of Al_2O_3 is TMA pulse/purge/H_2O pulse/purge for periods of 0.2 s/35 s/0.2 s/35 s. The coating thickness can be manipulated by controlling ALD deposition cycles.

5.3 | Cells Assembly

To make the solid-state lithium asymmetric cells, 80 mg of solid electrolytes were uniaxially pressed into a 10 mm-thick pellet with a diameter of 10 mm under 380 MPa in a homemade model cell (generally, the thickness of pellets is around 0.6 mm). Then Li and In foils were attached on one side of the SSE pellets and then pressed at 50 MPa. The formed Li/SSE/In cell was then sandwiched between two stainless-steel rods. The cells were assembled in an ultra-pure argon-filled glove box. For the preparation of cathode composites, we ground commercial LCO in conjunction with the as-synthesized Li_3InCl_6 at a weight ratio of 70:30. For cell fabrication, 80 mg Li_3InCl_6 powder and 50 mg LPSC and were pressed at 380 MPa. Subsequently, 10 mg of the cathode composite powder was dispersed on one side of the electrolyte and pressed again at 300 MPa. Then the In or Li/In foil was placed on the other side with a pressure of 50 MPa to ensure a good contact.

5.4 | Electrochemistry Test

The Li stripping/plating studies were carried out using NEWARE battery analyzers with a voltage range of 0–1.5 V and a current range of 0.1–5 mA·cm^{-2} at room temperature. Galvanostatic cycling was employed to evaluate the long cycling stability and the

critical current density. The long cycling test is conducted under constant current densities during repeated 1 h stripping/plating while the potential is recorded over time. In a typical electrochemical test, the cut-off voltage of stripping from In was set to 1.5 V. All-solid-state lithium metal cells were cycled in a galvanostatic mode (that is, a constant current protocol) within the voltage range of 2.1–3.6 V (vs Li$^+$/Li).

5.5 | Phase Characterization

Cycled cells were detached in the argon-filled glovebox, and electrodes were fully removed from the electrolytes. The surface of SSE is directly observed after peeling off the electrodes. Scanning electron microscope (SEM) images were obtained by using a Hitachi S-4800 field-emission scanning electron microscope (FE-SEM, acceleration voltage 5 kV).

5.6 | Calculation of Diffusion Coefficient

The diffusion behavior was investigated using the galvanostatic intermittent titration technique (GITT). In lithium alloy systems, the relaxation processes are primarily governed by the diffusion of lithium atoms. The lithium diffusion coefficient was estimated based on Fick's law, using the following simplified equations: (Equations (1) and (2))

$$D_{GITT} = \frac{4}{\pi\tau}\left(\frac{n_m V_m}{S}\right)^2\left(\frac{\Delta E_s}{\Delta E_t}\right)^2 \tag{1}$$

$$\tau \ll \frac{L^2}{D_{GITT}} \tag{2}$$

where τ represents the relaxation time, nm represents the mole value, and V_m is the mole volume, S is the contact area of electrode/electrolyte, ΔE_s is the voltage response stimulated by the pulse current, and ΔE_t is the voltage change by the galvanostatic discharge, L is the diffusion length (approximately the thickness here).

Conflicts of Interest

The authors declare no conflicts of interest.

Data Availability Statement

The data that support the findings of this study are available on request from the corresponding author. The data are not publicly available due to privacy or ethical restrictions.

References

1. J. A. Lewis, K. A. Cavallaro, Y. Liu, and M. T. McDowell, "The Promise of Alloy Anodes For Solid-State Batteries," *Joule* 6 (2022): 1418–1430, https://doi.org/10.1016/j.joule.2022.05.016.

2. T. Famprikis, P. Canepa, J. A. Dawson, M. S. Islam, and C. Masquelier, "Fundamentals of Inorganic Solid-State Electrolytes for Batteries," *Nature Materials* 18 (2019): 1278–1291, https://doi.org/10.1038/s41563-019-0431-3.

3. X. Li, J. Liang, X. Yang, et al., "Progress and Perspectives on Halide Lithium Conductors for All-Solid-State Lithium Batteries," *Energy & Environmental Science* 13 (2020): 1429–1461, https://doi.org/10.1039/C9EE03828K.

4. X. Li, J. Liang, J. Luo, et al., "Air-Stable Li$_3$ InCl$_6$ Electrolyte With High Voltage Compatibility For All-Solid-State Batteries," *Energy & Environmental Science* 12 (2019): 2665–2671, https://doi.org/10.1039/C9EE02311A.

5. J. Fu, S. Wang, J. Liang, et al., "Superionic Conducting Halide Frameworks Enabled by Interface-Bonded Halides," *Journal of the American Chemical Society* 145 (2023): 2183–2194, https://doi.org/10.1021/jacs.2c09446.

6. L. Zhou, C. Y. Kwok, A. Shyamsunder, Q. Zhang, X. Wu, and L. F. Nazar, "A New Halospinel Superionic Conductor For High-Voltage All Solid State Lithium Batteries," *Energy & Environmental Science* 13 (2020): 2056–2063, https://doi.org/10.1039/D0EE01017K.

7. Y.-C. Yin, J.-T. Yang, J.-D. Luo, et al., "A LaCl$_3$-Based Lithium Superionic Conductor Compatible With Lithium Metal," *Nature* 616 (2023): 77–83, https://doi.org/10.1038/s41586-023-05899-8.

8. X. Li, J. Liang, N. Chen, et al., "Water-Mediated Synthesis of a Superionic Halide Solid Electrolyte," *Angewandte Chemie International Edition* 58 (2019): 16427–16432, https://doi.org/10.1002/anie.201909805.

9. M. J. Wang, E. Kazyak, N. P. Dasgupta, and J. Sakamoto, "Transitioning Solid-State Batteries From Lab to Market: Linking Electro-Chemo-Mechanics With Practical Considerations," *Joule* 5 (2021): 1371–1390, https://doi.org/10.1016/j.joule.2021.04.001.

10. Y. Li, J. Li, H. Xiao, et al., "A Novel 3D Li/Li$_9$ Al$_4$ /Li-Mg Alloy Anode for Superior Lithium Metal Batteries," *Advanced Functional Materials* 33 (2023): 2213905, https://doi.org/10.1002/adfm.202213905.

11. J. Liang, X. Li, Y. Zhao, et al., "An Air-Stable and Dendrite-Free Li Anode for Highly Stable All-Solid-State Sulfide-Based Li Batteries," *Advanced Energy Materials* 9 (2019): 1902125, https://doi.org/10.1002/aenm.201902125.

12. G. A. Collins, H. Geaney, and K. M. Ryan, "Alternative Anodes for Low Temperature Lithium-Ion Batteries," *Journal of Materials Chemistry A* 9 (2021): 14172–, https://doi.org/10.1039/D1TA00998B.

13. Y. Zhong, X. Yang, R. Guo, et al., "Protecting Lithium Metal Anodes in Solid-State Batteries," *Electrochemical Energy Reviews* 7 (2024): 30, https://doi.org/10.1007/s41918-024-00230-z.

14. Y.-G. Lee, S. Fujiki, C. Jung, et al., "High-Energy Long-Cycling All-Solid-State Lithium Metal Batteries Enabled By Silver–Carbon Composite Anodes," *Nature Energy* 5 (2020): 299–308, https://doi.org/10.1038/s41560-020-0575-z.

15. D. H. S. Tan, Y.-T. Chen, H. Yang, et al., "Carbon-Free High-Loading Silicon Anodes Enabled By Sulfide Solid Electrolytes," *Science* 373 (2021): 1494–1499, https://doi.org/10.1126/science.abg7217.

16. D. Spencer-Jolly, V. Agarwal, C. Doerrer, et al., "Structural Changes in the Silver-Carbon Composite Anode Interlayer of Solid-State Batteries," *Joule* 7 (2023): 503–514, https://doi.org/10.1016/j.joule.2023.02.001.

17. J. Li, H. Su, Y. Liu, Y. Zhong, X. Wang, and J. Tu, "Li Alloys in All Solid-State Lithium Batteries: A Review of Fundamentals and Applications," *Electrochemical Energy Reviews* 7 (2024): 18, https://doi.org/10.1007/s41918-024-00221-0.

18. S. H. Lee, M. S. Kim, J.-H. Lee, et al., "A Li–In Alloy Anode and Nb$_2$ CT X Artificial Solid-Electrolyte Interphase For Practical Li Metal Batteries,"

Journal of Materials Chemistry A 10 (2022): 4157–4169, https://doi.org/10.1039/D1TA09366E.

19. X. Gu, J. Dong, and C. Lai, "Li-Containing Alloys Beneficial for Stabilizing Lithium Anode: A Review," *Engineering Reports* 3 (2021): 12339.

20. S. Luo, Z. Wang, X. Li, et al., "Growth of Lithium-Indium Dendrites In All-Solid-State Lithium-Based Batteries With Sulfide Electrolytes," *Nature Communications* 12 (2021): 6968, https://doi.org/10.1038/s41467-021-27311-7.

21. Y. Lu, C.-Z. Zhao, R. Zhang, et al., "The Carrier Transition From Li Atoms To Li Vacancies In Solid-State Lithium Alloy Anodes," *Science Advances* 7 (2021): abi5520, https://doi.org/10.1126/sciadv.abi5520.

22. T. Krauskopf, B. Mogwitz, C. Rosenbach, W. G. Zeier, and J. Janek, "Diffusion Limitation of Lithium Metal and Li–Mg Alloy Anodes on LLZO Type Solid Electrolytes as a Function of Temperature and Pressure," *Advanced Energy Materials* 9 (2019): 1902568, https://doi.org/10.1002/aenm.201902568.

23. C. Wang, T. Deng, X. Fan, et al., "Identifying Soft Breakdown In All-Solid-State Lithium Battery," *Joule* 6 (2022): 1770–1781, https://doi.org/10.1016/j.joule.2022.05.020.

24. D. Cao, K. Zhang, W. Li, et al., "Nondestructively Visualizing and Understanding the Mechano-Electro-chemical Origins of "Soft Short" and "Creeping" in All-Solid-State Batteries," *Advanced Functional Materials* 33 (2023): 2307998, https://doi.org/10.1002/adfm.202307998.

25. M. J. Counihan, K. S. Chavan, P. Barai, et al., "The Phantom Menace of Dynamic Soft-Shorts In Solid-State Battery Research," *Joule* 8 (2024): 64–90, https://doi.org/10.1016/j.joule.2023.11.007.

26. Z. Wang, J. Zhao, X. Zhang, et al., "Tailoring Lithium Concentration In Alloy Anodes For Long Cycling And High Areal Capacity In Sulfide-Based All Solid-State Batteries," *eScience* 3 (2023): 100087, https://doi.org/10.1016/j.esci.2022.100087.

27. C. Yu, Y. Li, K. R. Adair, et al., "Tuning Ionic Conductivity And Electrode Compatibility of Li_3YBr_6 for High-Performance All Solid-State Li Batteries," *Nano Energy* 77 (2020): 105097, https://doi.org/10.1016/j.nanoen.2020.105097.

28. J. Kasemchainan, S. Zekoll, D. Spencer Jolly, et al., "Critical Stripping Current Leads to Dendrite Formation On Plating In Lithium Anode Solid Electrolyte Cells," *Nature Materials* 18 (2019): 1105–1111, https://doi.org/10.1038/s41563-019-0438-9.

29. Z. Ning, D. S. Jolly, G. Li, et al., "Visualizing Plating-Induced Cracking In Lithium-Anode Solid-Electrolyte Cells," *Nature Materials* 20 (2021): 1121–1129, https://doi.org/10.1038/s41563-021-00967-8.

30. S. Wenzel, S. J. Sedlmaier, C. Dietrich, W. G. Zeier, and J. Janek, "Interfacial Reactivity and Interphase Growth of Argyrodite Solid Electrolytes at Lithium Metal Electrodes," *Solid State Ionics* 318 (2018): 102–112, https://doi.org/10.1016/j.ssi.2017.07.005.

31. A. Pei, G. Zheng, F. Shi, Y. Li, and Y. Cui, "Nanoscale Nucleation and Growth of Electrodeposited Lithium Metal," *Nano Letters* 17 (2017): 1132–1139, https://doi.org/10.1021/acs.nanolett.6b04755.

32. J. Xiao, Q. Li, Y. Bi, et al., "Understanding and Applying Coulombic Efficiency In Lithium Metal Batteries," *Nature Energy* 5 (2020): 561–568, https://doi.org/10.1038/s41560-020-0648-z.

33. Y. Huang, B. Shao, Y. Wang, and F. Han, "Solid-State Silicon Anode With Extremely High Initial Coulombic Efficiency," *Energy & Environmental Science* 16 (2023): 1569–1580, https://doi.org/10.1039/D2EE04057C.

34. X. Ji, S. Hou, P. Wang, et al., "Solid-State Electrolyte Design for Lithium Dendrite Suppression," *Advanced Materials* 32 (2020): 2002741, https://doi.org/10.1002/adma.202002741.

35. H. Huo, M. Jiang, Y. Bai, et al., "Chemo-Mechanical Failure Mechanisms of the Silicon Anode In Solid-State Batteries," *Nature Materials* 23 (2024): 543–551, https://doi.org/10.1038/s41563-023-01792-x.

36. P.-L. Larsson, A. E. Giannakopoulos, E. SÖderlund, D. J. Rowcliffe, and R. Vestergaard, "Analysis of Berkovich Indentation," *International Journal of Solids and Structures* 33 (1996): 221–248, https://doi.org/10.1016/0020-7683(95)00033-7.

37. C. Hänsel, B. Singh, D. Kiwic, P. Canepa, and D. Kundu, "Favorable Interfacial Chemomechanics Enables Stable Cycling of High-Li-Content Li–In/Sn Anodes in Sulfide Electrolyte-Based Solid-State Batteries," *Chemistry of Materials* 33 (2021): 6029–6040, https://doi.org/10.1021/acs.chemmater.1c01431.

38. A. L. Santhosha, L. Medenbach, J. R. Buchheim, and P. Adelhelm, "The Indium– Lithium Electrode In Solid-State Lithium-Ion Batteries: Phase Formation, Redox Potentials, And Interface Stability," *Batteries & Supercaps* 2019, 2, 524–529.

Supporting Information

Additional supporting information can be found online in the Supporting Information section.

Supporting File: aenm70628-sup-0001-SuppMat.docx